




Weldability, microstructure, and residual stress in Al/Cu and Cu/Al friction stir spot weld joints with Zn interlayer

Adel Boucherit¹ · Said Abdi¹ · Mouloud Aissani² · Brahim Mehdi³ · Khadidja Abib³ · Riad Badji² 

Received: 16 June 2020 / Accepted: 29 September 2020 / Published online: 14 October 2020
© Springer-Verlag London Ltd., part of Springer Nature 2020

Abstract

In this work, the effect of lap joint configuration and Zn interlayer addition on the microstructure, the residual stress state, and the quality of Al/Cu (configuration #1) and Cu/Al (configuration #2) friction stir spot welds (FSSW) was investigated. The study revealed the close dependency of the weld joint quality on the pin length and Zn addition. The higher the pin plunge depth is, the greater the obtained tensile shear strength. The Zn addition reduced sensibly the thickness of Al₂Cu layer (from 10 to 2 μm) and favored the formation of the Al_{4.2}Cu_{3.2}Zn_{0.7} precipitate that hindered the formation of detrimental Al₄Cu₉ compounds. Material flow analysis revealed the presence of an intermixing zone containing thin continuous intermetallic layer (approximately 2.07 μm) at the weld interface of configuration #1. Meanwhile, the Cu material was covered by the Zn layer, which resulted in a hardness increase (228 HV) at the stirred zone. In addition, a significant increase of the tensile shear strength from 1650 to 3600 N was noticed (an improvement rate of ≈ 118%). Conversely, in configuration #2, the Zn foil was squeezed out of the spot weld interface resulting in the absence of material intermixing, discontinuous intermetallic layer, low hardness level (140 HV), and weak improvement rate of the shear strength (≈ 53%). The Zn interlayer addition resulted in a quasi-symmetric distribution of the residual stresses and shifted their nature from tensile stresses (+ 60 MPa) to compressive ones (− 10 MPa).

Keywords FSSW · Aluminum · Copper · Zinc interlayer · Tensile shear · Microstructure · Intermetallic compounds · Residual stress

1 Introduction

The dissimilar joining of aluminum (Al) to copper (Cu) is increasing more and more in many industrial fields such as electric power, aerospace, and ship-building owing to the outstanding mechanical and thermal properties, as well as the good corrosion resistance of these materials [1–5]. It has been suggested that Cu should be replaced by Al due to its cost-effectiveness and considerable mass reduction [6]. Besides,

joining both materials using conventional fusion welding is fairly challenging because of the formation of brittle intermetallic compounds (IMCs) and the solidification defects such as porosities and chemical segregations. This compromises the mechanical properties of the weld joint mainly if the IMCs' fraction within the microstructure is high and their average size exceeds 2.5 μm [7]. From a technological viewpoint, fusion processes are not suitable for such materials, as they generate solidification defects that decrease the weld joint performances. However, solid-state joining processes are known to reduce the IMCs' formation within the microstructure. The literature reports some papers that deal with the joining of Al to Cu using FSSW. Recently, Pandey et al. [8] investigated the influence of welding parameters such as tool rotation speed, pin tool profile, welding speed, and tool offset position on FSW of aluminum alloys. They indicated that both the tool rotational speed increase and the threaded pin tool result in high heat generation and enhancement of material flow. This improves the tensile strength and the ductility of the weld joint [8]. On the other hand, Gaohui et al. [9] studied the effect of dwell time parameter and concluded that the tensile shear

✉ Riad Badji
riadbadji@gmail.com; r.badji@crti.dz

¹ Laboratoire des Sciences et de Génie des Matériaux, LSGM, Université des Sciences et de la Technologie Houari Boumediene, USTHB, Algiers, Algeria

² Research Center in Industrial Technologies CRTI, P.O. Box 64, Cheraga, 16014 Algiers, Algeria

³ Laboratoire de Physique des Matériaux, Faculté de Physique, Université des Sciences et de la Technologie Houari Boumediene USTHB, B.P. 32, El-Alia, Bab-Ezzouar, DZ-16111 Algiers, Algeria

failure increases when increasing dwell time in the interval of 1 to 5 s. A further increase of the dwell time up to 9 s decreases the tensile shear strength. Gaohui et al. [9] revealed the presence of brittle and harmful Al_2Cu , AlCu , and Al_4Cu_9 precipitates at the interface of Al/Cu FSSW joints. They noticed a close dependency of the tensile shear strength on the dwell time. Similarly, Shiraly et al. [10] concluded that the tensile shear strength of Al/Cu FSSW joints increases with the tool rotation speed. They obtained an optimal value of the tensile shear strength for 1400 rpm tool rotation speed. Heideman et al. [11] investigated the effect of both the pin length and tool rotation speed on the microstructure of Al/Cu FSSW joints. They concluded that the rotation speed has the most significant effect on the weld strength while the average weld strength increases with the pin rotation speed. It should be noted that several IMCs have been identified after friction stir welding (FSW) and FSSW of Al to Cu, such as Al_2Cu and Al_4Cu_9 [9, 12–15], AlCu [9, 12, 16–18], Al_2Cu_3 [12, 19], and AlCu_3 [10, 12]. The size and amount of these IMCs are crucial factors that may control the mechanical behavior of the FSSW joint. The formation of intermetallic layer depends on both the operating conditions and the welding process being used. Zhang et al. [20] highlighted the presence of a thick intermetallic layer of 18 μm in a Cu/Al FSW lap joint, while Xue et al. [15, 21] revealed the presence of 3 μm continuous IMC layer. The main conclusion of these studies was that the weld joint quality is affected when the intermetallic layer thickness exceeds 4 μm . In practice, the insertion of an interlayer is one of the technological solutions that were adopted to improve the FSSW weld joint quality. The chosen interlayer has to ensure the good material bonding and should modify the chemical reactions at the weld interface so that the final microstructures get improved. Moreover, it should control the kinetics of IMCs' formation to achieve better mechanical properties of the weld joint [22]. Saeid et al. [23] studied the FSW of Al/Cu and revealed the presence of brittle Al_2Cu and Al_4Cu_9 IMCs that led to the formation of microcracks and destroyed the weld joint quality. They demonstrated that the use of Zn interlayer at the Al/Cu joint interface reduces the size and amount of the harmful IMCs and improves the strength and ductility of the weld joint.

For the dissimilar joining of Al to Cu, the Zn foil was chosen owing to its chemical affinity with these elements, relatively, at high temperatures, as indicated by the binary phase diagrams of Al-Zn and Cu-Zn [24, 25]. Several authors have examined the use of a Zn foil at the interface between Cu and Al and highlighted its beneficial effect on the weld joint quality [22, 26–29]. The insertion of a thin Zn foil at the Al/Cu FSSW weld joints interface leads to significant improvement of their tensile behavior through the reduction of the harmful IMCs amount within the microstructure [29]. The insertion of Zn between Al and Cu enhances the competition regarding the formation of Cu_xZn_y , Al_xCu_y , or $\text{Al}_x\text{Cu}_y\text{Zn}_z$ compounds [22,

26]. This is due to the high chemical affinity between Zn and Cu, which will subsequently limit the formation of Al_xCu_y intermetallic compounds.

Chang et al. [30] noticed that the use of Ni interlayer prevents the formation of $\text{Al}_{12}\text{Mg}_{17}$ IMC and enhances the tensile strength of Al/Mg dissimilar joint of about 66%. In their recent work, Chatterjee et al. [31] examined the effect of Cu interlayer on both the microstructure and mechanical properties of the dissimilar NiTi/Ti6Al4V laser weld joint. They concluded that the Cu addition favors the formation of Cu_4Ti_3 and CuNi_2Ti compounds, improves the tensile strength, and prevents the precipitation of brittle Ti_2Ni , Ti_3Ni_4 , and TiO_2 IMCs. The same authors [32] improved the mechanical properties of AISI 316/NiTi dissimilar weld joint through Cu interlayer addition that reduced sensibly the amount of brittle IMCs.

Up to date, many research papers are dealing with the joining of Al and Cu using several processes. However, only few information are available concerning the joining of these materials using the FSSW process, namely, the effect weld joint configuration on the weld joint quality and residual stress state. Thus, this work is a contribution to a good understanding of the dissimilar joining of Al to Cu using different lap FSSW joint configurations. The effect of Zn introduction (as a filler metal) on microstructure and weld joint quality has been examined. Special attention was given to precipitation phenomena and their effect on the mechanical behavior of the weld joint. The resulting residual stresses' (RSs) state was analyzed and correlated to the process parameters. The effect of these RSs, on the mechanical properties (namely hardness) of the weld joint, was examined.

2 Materials and experimental procedures

The materials used in this study are sheets of aluminum (Al 1050, 99.50 wt%) and copper (Cu a-1, 99.9 wt%) of 2 mm and 5 mm thicknesses respectively. These materials were joined using FSSW process with a 0.2-mm-thick Zn interlayer at the sheet interface. Two experimental configurations were adopted as illustrated in Fig. 1. The first configuration shows the Al sheet in the upper position of the lap joint and the Cu in the lower one (Fig. 1a). The situation was inverted in the second configuration (Fig. 1b).

For both materials, sheets of $75 \times 25 \text{ mm}^2$ were prepared and joined with and without a Zn interlayer. The prepared sheets were positioned and fixed on a holder made of XC20 steel and fired as illustrated in Fig. 2a. A designed welding tool (made of H13 tool steel) containing a conical retractable pin [33] was used. The position of the conical pin can be adjusted by a suitable clamping bolt in the shoulder depending on its active length. For configuration #1, the spot welds were carried out using four different pin lengths as indicated in Fig.

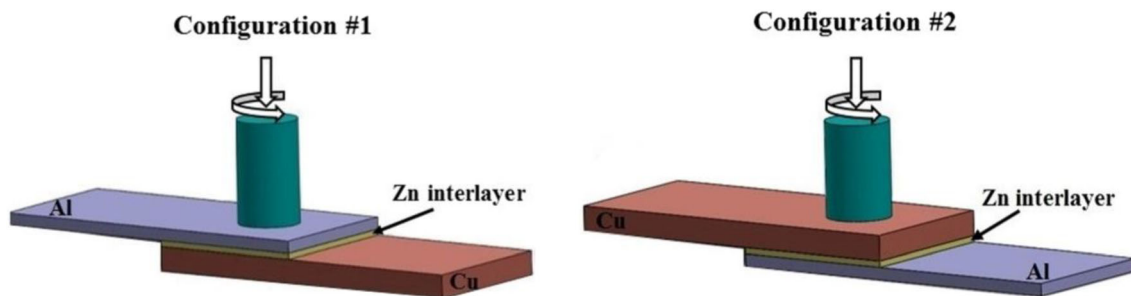


Fig. 1 Schematic illustration of employed FSSW lap joints. a Configuration #1. b Configuration #2

2b whereas only one pin length (6 mm) was adopted for configuration #2.

The appellation of each welding test includes the letter “P” (penetration) and the corresponding pin length; for example, P6 corresponds to the weld performed with 6 mm pin length. The welds were performed in the same conditions: with a dwell time of 4 s (the time after the rotating tool was plunged into the surface) and a rotational speed of 1400 rpm. The experimental parameters’ details are given in Table 1.

After the welding process, transverse sections were prepared from the several welding conditions for microstructural analysis. The specimens were mechanically polished with silicon carbide paper down to grade 4000 then with 3 and 1 μm diamond paste on polishing clothes. They were then electropolished using (400 ml H₃PO₄, 600 ml H₂O) and (20 ml fluoroboric acid in distilled water) for copper and aluminum respectively. Detailed microstructural analysis was done using an Olympus BX41 optical microscope and a ZEISS Gemini

500 scanning electron microscope (SEM) operating at 15 kV and equipped with energy-dispersive spectroscopy system (EDS-Oxford). The mechanical properties of the different weld joints were evaluated using tensile shear tests. The dimensions and the design of the specimens are shown in Fig. 3a. For each welding parameter, four shear tests were performed on an INSTRON universal 50982 tensile testing machine at a strain rate of $2.6 \cdot 10^{-4} \text{ s}^{-1}$. Microhardness measurements were performed on transverse sections of the specimens using a Buehler® microindenter with 50 g load and 15 s indentation time. In order to map the microhardness, indentations were spaced at a regular interval of 0.25 mm along several horizontal lines throughout the weld joint thickness. The data were, then, introduced in the “tecplot” software that allowed the hardness mapping. X-ray diffraction (XRD) patterns were recorded on a Bruker D8 DISCOVER diffractometer operating at 45 kV and 40 mA using Cu-Kα radiation ($\lambda = 1.54 \text{ \AA}$). The diffraction patterns were collected in the

Fig. 2 Schematic illustration of a sheets’ fixture setup and b retractable threaded conical pins and pinless tool

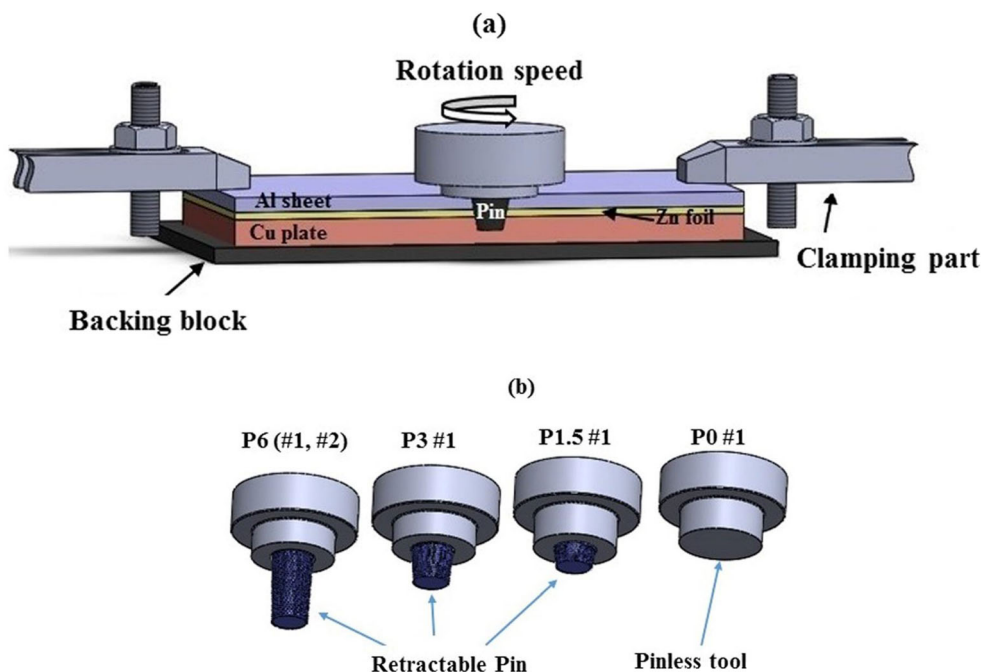


Table 1 Summary of the used process parameters

| Spot weld | Pin plunge depth (mm) | Configuration | Nomenclature of specimens | | Rotational speed (rpm) | Dwell time (s) |
|-----------|-----------------------|---------------|---------------------------|----------|------------------------|----------------|
| | | | Without Zn | With Zn | | |
| Al/Cu | 6 | #1 | P6 | P6-Zn | 1400 | 4 |
| Al/Cu | 3 | #1 | P3 | P3-Zn | Idem | Idem |
| Al/Cu | 1.5 | #1 | P1.5 | P1.5-Zn | - | - |
| Al/Cu | 0 | #1 | P0 | P0-Zn | - | - |
| Cu/Al | 6 | #2 | P6#2 | P6-Zn-#2 | - | - |

range of $20\text{--}120^\circ$ in 2θ with a step size of 0.02° . The peak indexation was performed using the PDF4 crystallographic database within EVA software. Residual stresses (RSs) analysis was performed by means of the $\sin^2\psi$ method, in line with [34] following the methodology given in the NF EN 15305 European standard [35]. The X-ray diffractometer was calibrated using a set of Al and Cu standards. For these measurements, twenty angles varying from -70° to $+70^\circ$ were chosen. The $\varepsilon_{\phi\psi}$ strain was evaluated with the $\{4\ 2\ 0\}$ atomic plane situated at $2\theta = 144^\circ$ for Cu and with $\{4\ 2\ 2\}$ one at $2\theta = 138^\circ$ for Al. The RSs were estimated using elastic constants: the Young modulus ($E_{\text{Cu}} = 100$ GPa, $E_{\text{Al}} = 71$ GPa), Poisson

coefficient ($\nu_{\text{Cu}} = 0.3$, $\nu_{\text{Al}} = 0.3$), and anisotropic factor (ARX = 1).

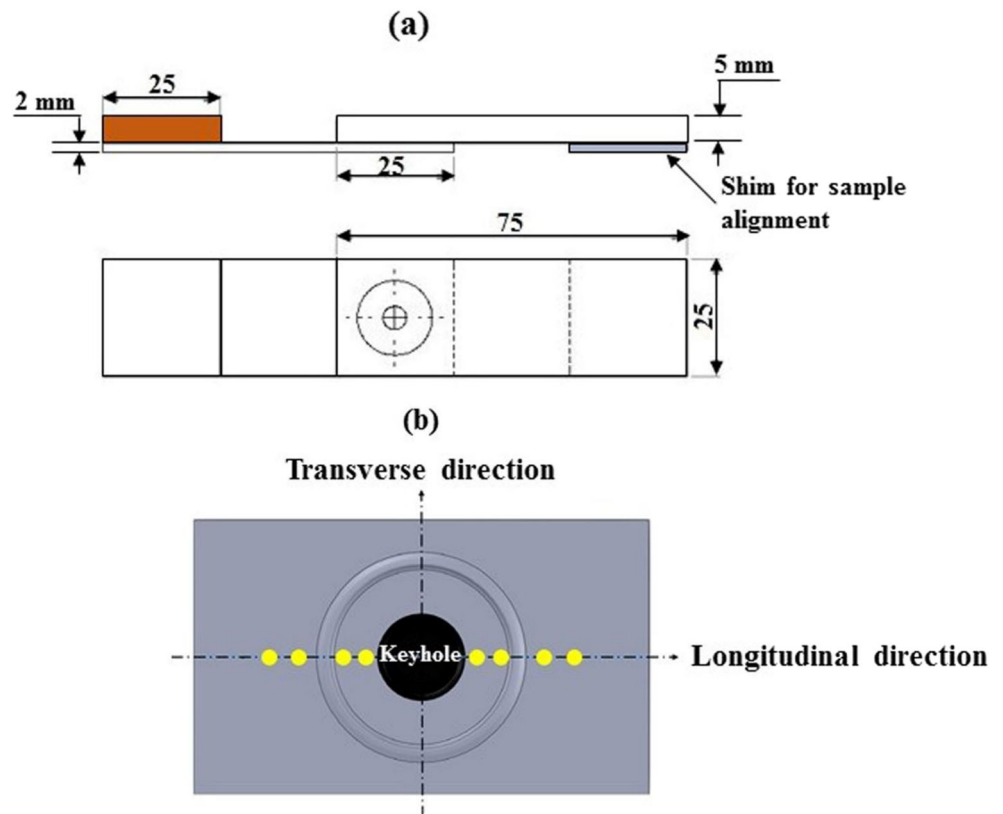
In order to determinate the RSs values, the following equations were used:

The strain ε_{hkl} can be given by Eq. (1):

$$\varepsilon_{\text{hkl}} = \frac{d_{\text{hkl}} - d_0}{d_0} \quad (1)$$

where d_0 is the lattice spacing of a stress-free plane. In order to determine the RSs in the longitudinal and transversal directions, measurements should be done in several directions,

Fig. 3 **a** Geometry and dimensions of tensile shear specimen. **b** Positions of residual stresses measurements



characterized by the ψ angles. The values of these various directions can, then, be used to derive the RSs.

The basic equation for the stress calculation is given as follows:

$$\begin{aligned} \frac{d_{hkl}-d_o}{d_o} = & \frac{1}{2}s_2(\sigma_{11}\cos^2\varphi + \sigma_{12}\sin 2\varphi + \sigma_{22}\sin^2\varphi - \sigma_{33})\sin^2\Psi \\ & + \frac{1}{2}s_2\sigma_{33} + s_1(\sigma_{11} + \sigma_{22} + \sigma_{33}) \\ & + \frac{1}{2}s_2(\sigma_{13}\cos\varphi + \sigma_{23}\sin\varphi)\sin 2\Psi \end{aligned} \quad (2)$$

where s_1 and $\frac{1}{2}s_2$ are the diffraction elastic constants given in Eqs. (3) and (4).

$$s_1 = \frac{-\nu}{E} \quad (3)$$

$$\frac{1}{2}s_2 = \frac{1+\nu}{E} \quad (4)$$

E and ν are Young's modulus and Poisson's ratio respectively.

The longitudinal and transversal RSs were analyzed in parallel and perpendicularly to the sheets' rolling directions respectively. The XRD penetration depth for stress determination was about 20 μm . All the collected data were analyzed using LEPTOSTM software. The chosen positions for RSs measurements in a typical sample are shown in Fig. 3b.

3 Results and discussion

3.1 Effect of process parameters on the FSSW weld joint quality

Figure 4 illustrates the microstructures of both Al and Cu base metals (BMs). The Al microstructure exhibits elongated grain morphology (Fig. 4a) according to the rolling direction of the sheet. The Cu microstructure exhibits quasi-equiaxed grain

morphology due to their recrystallized state (Fig. 4b). The corresponding average grain sizes were 215 μm and 28 μm for Al and Cu respectively.

The macrographic views of the transverse cross sections of the different weld joints obtained from configuration 1 are depicted in Fig. 5a–h. A qualitative visual inspection of the welds indicated the absence of apparent defects, except for the P0 #1 sample without Zn interlayer that was not joined due to lack of heat input, at the sheet interface, as shown in Fig. 5h. A clear variation of the keyhole morphology according to the pin length can be noticed through Fig. 5a–h. For the configuration #1, a specific shape is observed at the sheet interface for pin lengths of 3 and 6 mm as illustrated in Fig. 5a–d. During the plunging movement of the pin, the Al material was pushed downward, and the Cu sheet was gradually extruded upward into the upper side of the Al one, because of the Cu plastic flow, which led to the formation of the swirl flow. This shape is labeled in the present work as “hook ring.” A similar shape, called “copper ring,” was previously reported in the literature [11, 12]. The macrographs corresponding to configuration #2 for 6 mm pin length are shown in Fig. 5i–j.

The figures show a stamping of the Cu sheet within the Al one without materials' intermixing at the interface. This behavior is due to the difference in the mechanical properties of Cu and Al, especially their hardness. Figure 6a, b shows the tensile shear testing results for the different process parameters used in this study.

Table 2 summarizes the tensile shear properties determined from Fig. 6 for configurations #1 and #2 conducted using 6 mm pin length.

For both configurations, the FSSW joints, obtained using 6 mm pin length, depicted better tensile properties in comparison with other pin lengths. This can be attributed to the increased heat flow induced by the deep penetration of the pin (6 mm). In addition, the tensile properties of the weld joint, conducted using the Zn interlayer (Fig. 6b), were remarkably improved compared with those obtained without Zn (Fig. 6a). It should be noted that the FSSW joints obtained from configuration #1 exhibited better tensile properties than those of configuration #2. This is due to the creation of an important

Fig. 4 Optical micrographs of the as-received base materials. **a** Al and **b** Cu

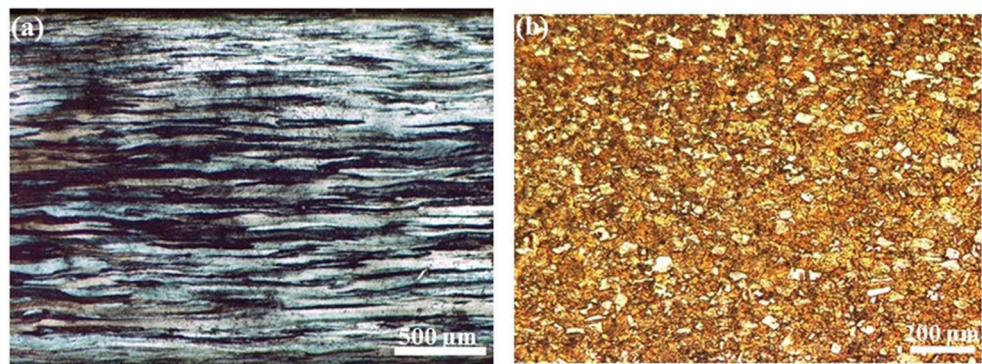
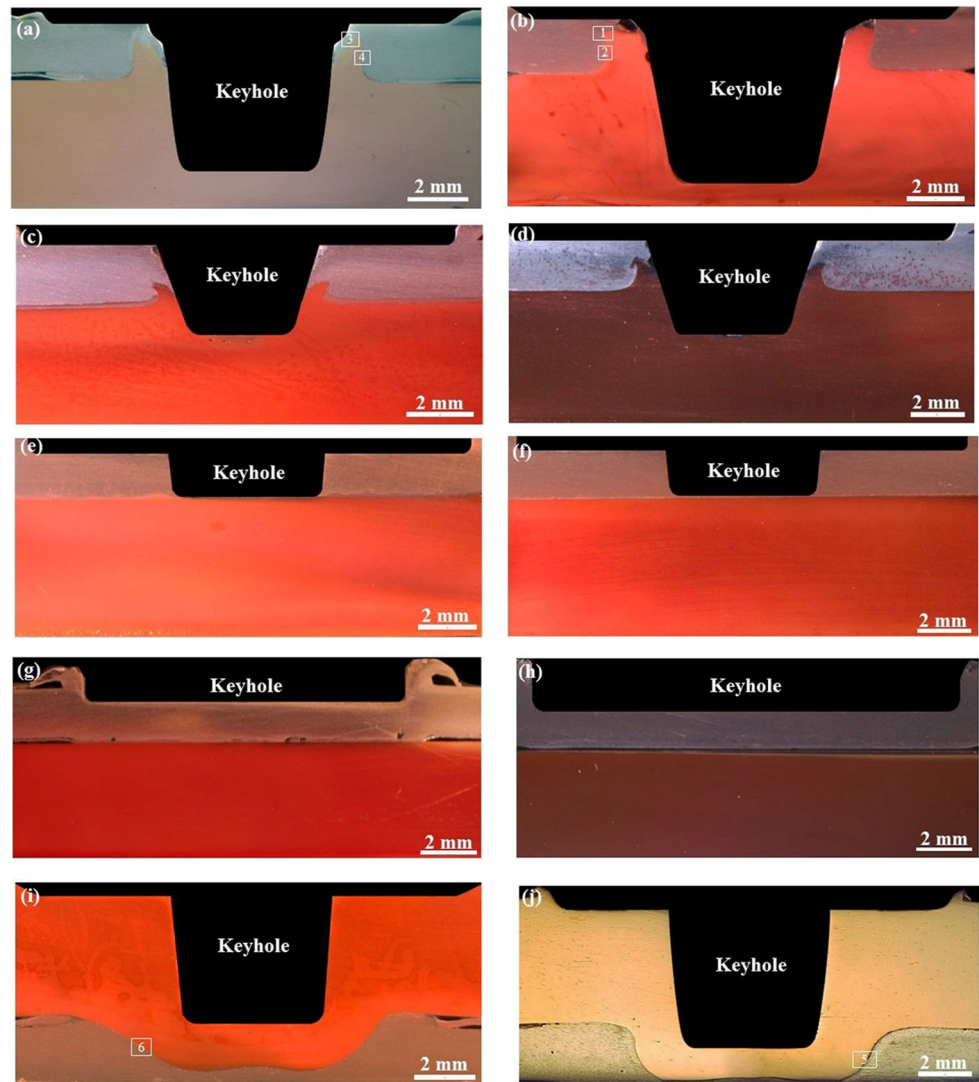


Fig. 5 Optical macrographs of FSSW joints. **a–h** Configuration #1. **i–j** Configuration #2



“hook ring” at the sheet interface as described before in Fig. 5a and b. Similar effect of the pin length on the FSSW joint

quality was reported in the literature [11]. The P0 #1 and P1.5 #1 FSSW joints showed insignificant tensile behavior

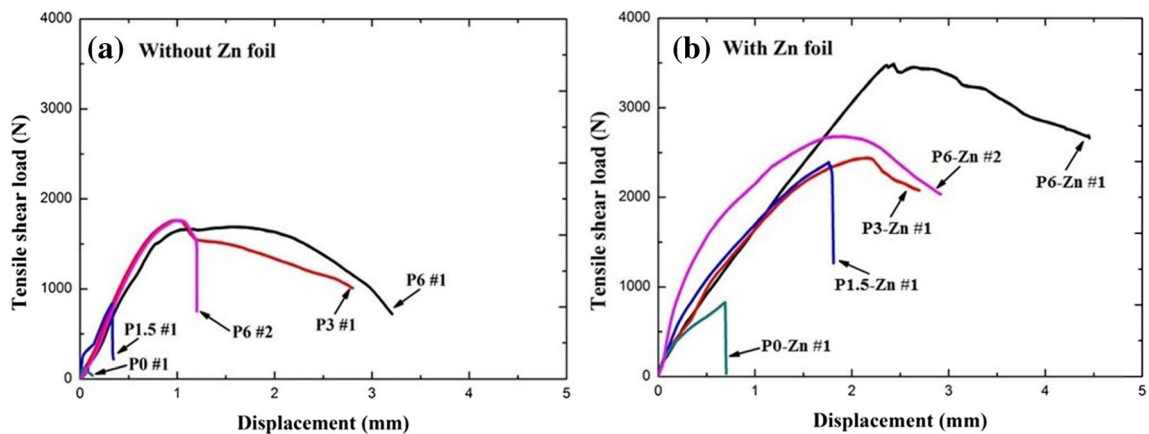


Fig. 6 Tensile shear testing load-displacement curves of the different FSSW joints **a** without Zn interlayer and **b** with Zn interlayer

Table 2 Tensile shear properties and fracture location for the different welding conditions

| Joint | P6-Zn #1 | P6 #1 | P6-Zn #2 | P6 #2 |
|---|-------------------|--------------------------|------------|--|
| Failure load (N) | 3600 ± 150 | 1650 ± 50 | 2750 ± 250 | 1800 ± 100 |
| Displacement at the onset of damage (mm) | 2.6 ± 0.5 | 1.1 ± 0.2 | 2 ± 0.3 | 1 ± 0.1 |
| Mean value of engineering strain at the onset of damage (%) | 3.5% | 1.4% | 2.6% | 1.3% |
| Fracture location | Plug failure mode | Interfacial failure mode | Al HAZ | Sharp decohesion at the Al/Cu interface (interfacial failure mode) |

due to the absence of materials' intermixing as described before. These results revealed the significant role of the Zn interlayer in the bonding of Cu and Al during the FSSW process. They also highlighted the beneficial effect of the “hook ring” on the tensile properties of the investigated dissimilar Cu/Al FSSW joints. In fact, when the softer metal (Al) was placed in the upper position of the dissimilar lap joint, the flow of the harder one (Cu) provoked the formation of a “hook ring” around the keyhole. This reinforced the tensile behavior of the weld joint during shear testing. These results are different from those published in the literature [36–39] for homogeneous FSSW joints, where the hook was considered as a source of crack initiation along its tip during loading. It can be noticed from Figs. 5 and 6 that the FSSW joints realized using 6 mm pin length exhibited the best shear properties and macroscopic appearance. Thus, only these cases will be considered for microstructural and mechanical behavior investigation in the rest of the paper.

Figure 7a–d shows macroscopic views of the fractured FSSW joints obtained using a 6-mm pin length after tensile shear testing. For both configurations, the weld joints conducted without Zn interlayer exhibited a typical interfacial failure mode characterized by a complete nugget de-bonding (Fig.

7a, c). However, the lap joints conducted using Zn interlayer revealed a better fracture behavior, called also “plug fracture mode” [40] (see Fig. 7b, d). In fact, the Zn addition improved the weld joint quality and prevented its total fracture during shear testing. In this case, the shear testing resulted in the formation of cracks at the edge of the hook ring tip (Fig. 7b and d). It should be noted that the crack size observed in the specimens obtained from configuration #1 (Fig. 7b) was less than that of the specimens obtained from configuration #2 (Fig. 7d). Figure 8a–e shows the fracture surfaces of FSSW joints obtained using 6 mm pin length for both configurations #1 and #2.

The fracture surfaces of the lap joints conducted without Zn interlayer were characterized by intense cracking phenomenon (Fig. 8a–d) in both Al and Cu materials. The observed cracking phenomenon was attributed to presence of brittle intermetallic compounds (IMCs) such as Al_4Cu_9 that were identified by EDS analysis. The presence of these intermetallic compounds in Al/Cu weld joint was considered as the major factor of their fracture during loading as reported by Zhao et al. [41]. (Detailed investigation of the precipitation phenomena is given in the next section). The fracture surface of the lap joint obtained using Zn interlayer (configuration #2)

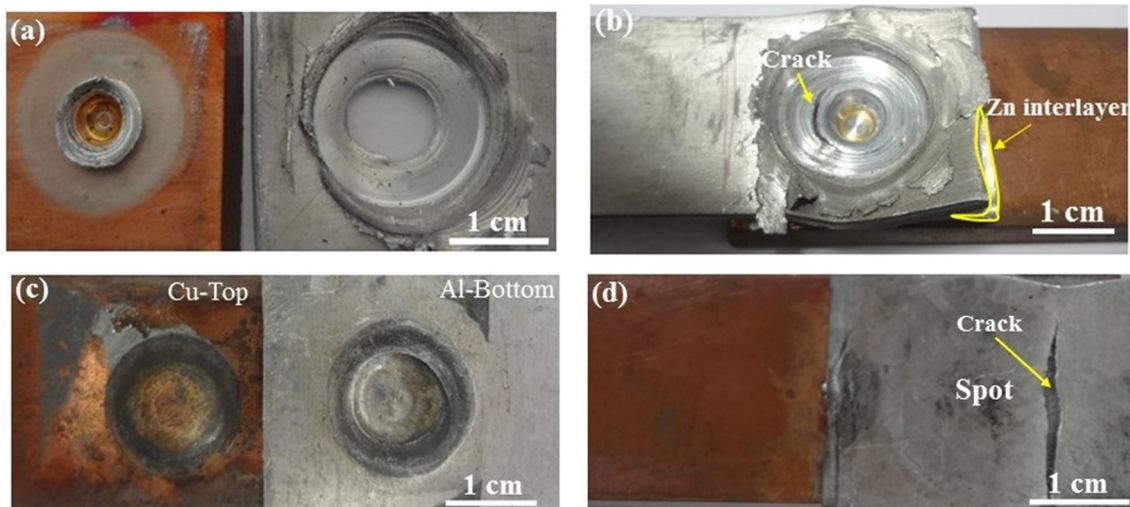


Fig. 7 Macroscopic views of fractured specimens prepared from P6 joints **a** and **c** without Zn and **b** and **d** with Zn interlayer for configurations #1 and #2 respectively

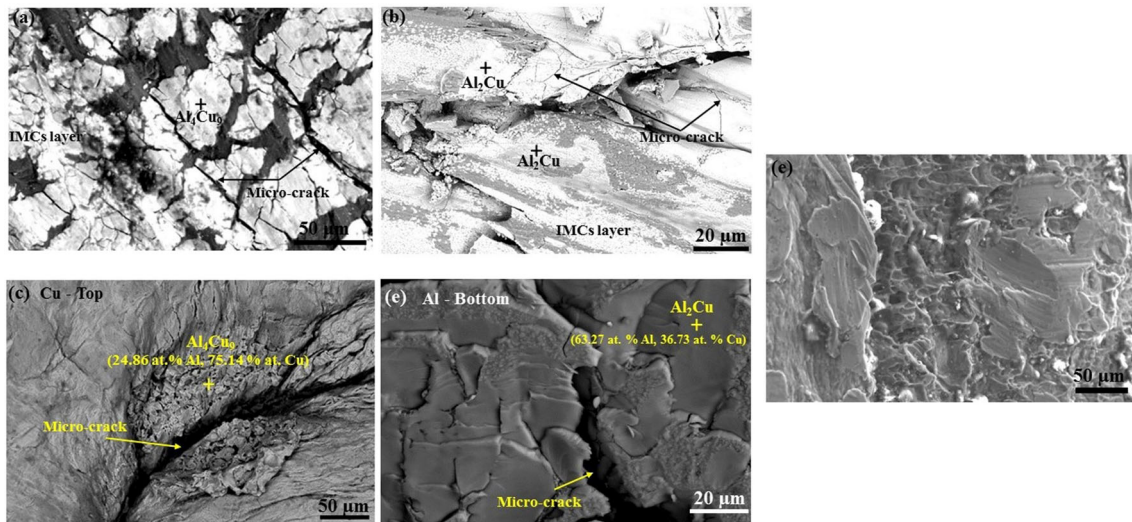


Fig. 8 a and b SEM fracture surfaces of the P6 joint (configuration #1) produced without Zn for Al and Cu respectively. c and d High magnification SEM fracture surfaces of the P6 joint (configuration #2) produced with Zn

produced without Zn for Al and Cu respectively. e High magnification SE fracture surface of the P6 joint (configuration #2) produced with Zn

revealed the presence of brittle areas and some dimples that characterize ductile fracture mode. These findings are in good agreement with those published by Lee et al. [18] and Han et al. [42]. These results support well the observations given in Fig. 7 and the tensile behavior given in Fig. 6. It should be noted that the fracture surface of the specimen shown in Fig. 7b (P6-Zn #1) was not presented in Fig. 8 as its failure was not achieved during the shear testing.

3.2 Microstructure and precipitation phenomena around the keyhole

The microstructural evolution around the keyhole is shown in Fig. 9a–e at low magnification. Based on the observed grain size and morphology, three main regions are distinguished: (i) the stirred zone (SZ), the thermomechanically affected zone (TMAZ), and the heat-affected zone (HAZ). The presented micrographs depict apparent change in the grain size and morphology across the different regions of the weld joint. This is due to the strong plastic deformation of the material during the stirring process.

A comparison between the configuration (#1) and (#2) led to highlight two types of stirred zones (SZ) around the keyhole. In configuration #1, the tool pin penetrated both Al and Cu sheets. Thus, two SZs were formed in both Al (Fig. 9a) and Cu (Fig. 9b). In configuration #2, the tool pin penetrated only the upper sheet (Cu). Thus, the SZ was generated only in Cu (Fig. 9c) because the Al sheet had no direct contact with the tool pin as shown in Fig. 9d. For this configuration, only the HAZ and the TMAZ were observed in the Al sheet as illustrated in Fig. 9e.

The microstructural evolution across the FSSW joint for the configuration #1 (with Zn interlayer) is given in

Fig. 10a–f. For the Al sheet, the SZ microstructure (Fig. 10a) was composed of highly refined grains compared with the other regions of the FSSW joint. This is due to the strong thermomechanical forging of the material coupled to the stirring action of the rotational movement of the welding tool. For the Cu sheet, the SZ microstructure (Fig. 10b) exhibited remarkable change in the grain size and morphology around the keyhole. In fact, the tool rotation movement combined to the forging force heat and stirred the parts of the joined materials at the pin vicinity.

This allows a strong grain fragmentation and formation of dislocation loops through intragranular slip mechanism leading to subgrain formation within the microstructure. Mimouni et al. [43] reported that the high plastic strain level resulting from the dislocation accumulation at the subgrain boundaries causes the rotation of these subgrains in relation to each other. According to Huang et al. [44], these dislocation loops are transformed to new recrystallized grains having various crystallographic orientations. It has been stated by several authors [16, 29, 45] that the fine grain microstructure of the nugget zone is formed through a continuous dynamic recrystallization process rather than a discontinuous dynamic recrystallization one. Su et al. [46] and Mroczka et al. [47] pointed out that, due to short time duration of the welding operation, the microstructure of the stirred zone is not completely restored at the end of the process and may contain dislocations with different structures and densities.

In addition, the figure illustrates clearly the vortex material flow caused by the pin rotation movement. It should be noted that this region contains islands of the Zn interlayer in the vortex central region. The TMAZ (narrow band between the stir zone and HAZ) of both Al (Fig. 10c) and Cu (Fig. 10d) is composed of deformed and fragmented grains that were

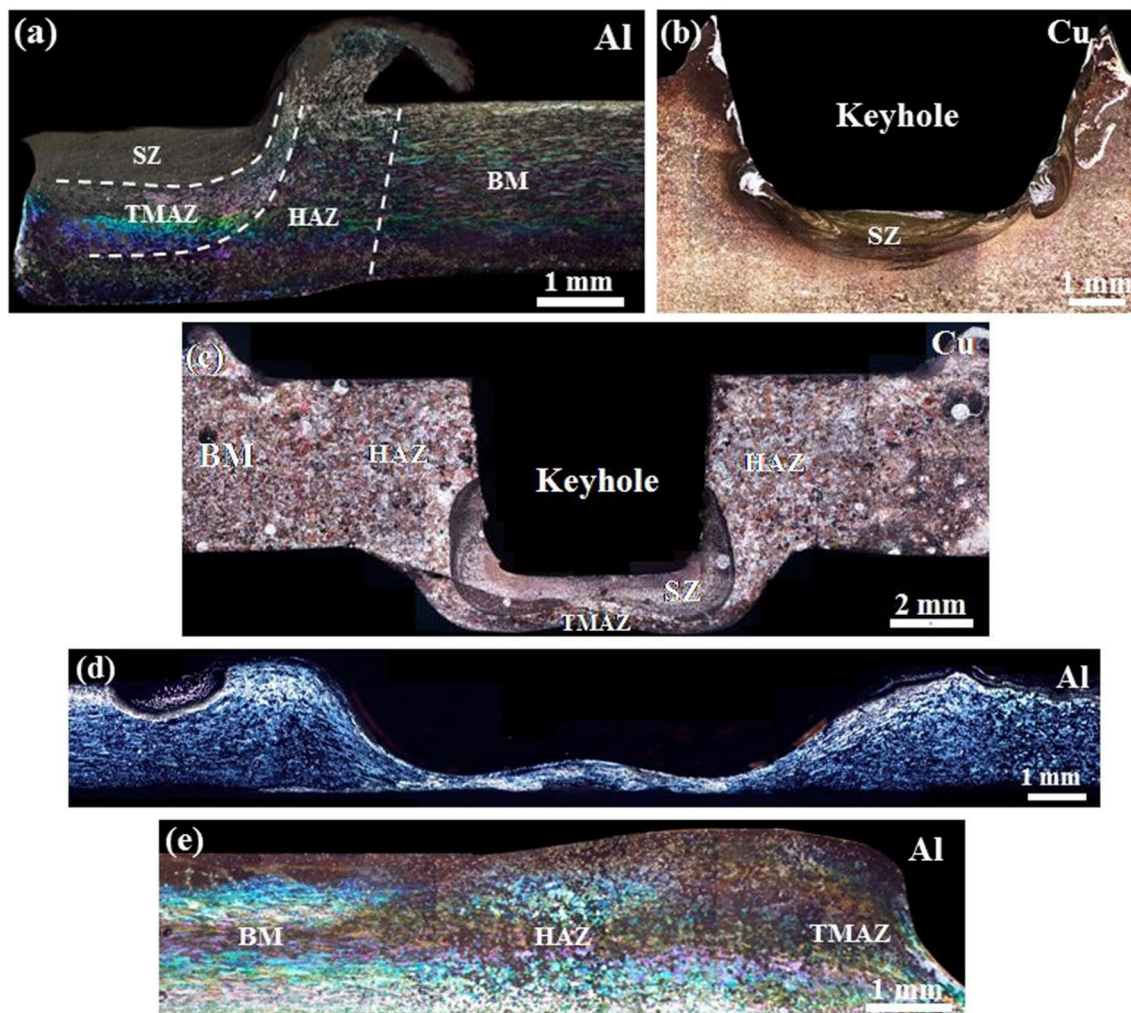


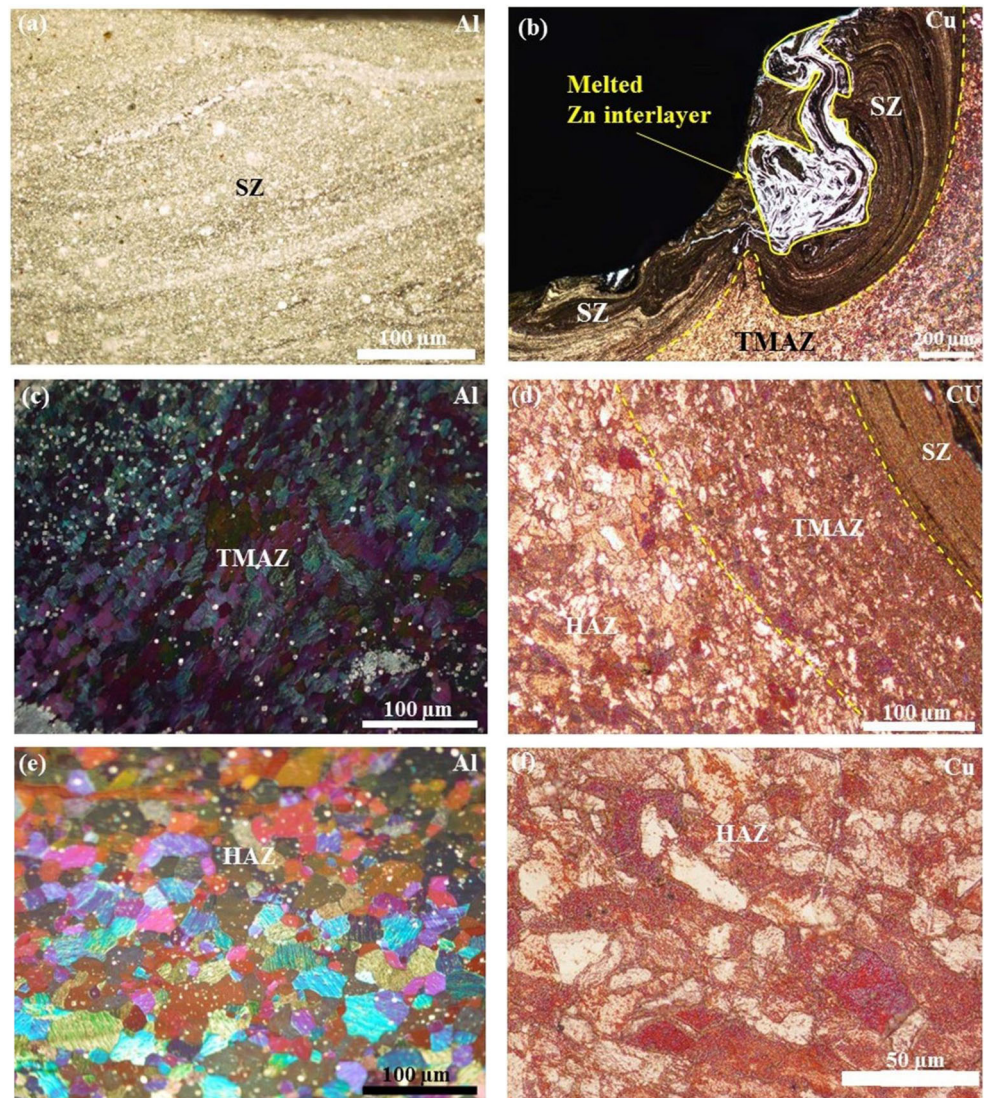
Fig. 9 Optical macrostructures (cross sections) of specimens prepared from **a** and **b** configuration #1 and **c–e** configuration #2

oriented according to the material flow. For both materials, a slight grain growth was recorded in this region compared with the SZ. In addition, the TMAZ microstructure is partially recovered as reported in other research works [16, 45]. The HAZ microstructures of both Al (Fig. 10e) and Cu (Fig. 10f) illustrate a clear grain growth in comparison with those of the SZ and TMAZ. This is attributed to the heat input generated during the pin rotation [37, 38]. For configuration #2, the microstructural changes concern mainly the copper material (Fig. 11a–c). From a morphological view point, the microstructural features depicted in this figure led to distinguish the following zones:

- (i) The SZ (Fig. 11a) that is composed of fine dynamically recrystallized grains resulting from both high temperature effect and intense plastic deformation caused by the pin rotation movement.
- (ii) The TMAZ (Fig. 11b) that contains highly deformed and fragmented grains resulting from the thermomechanical effect of the process.
- (iii) The HAZ (Fig. 11c) which is characterized by remarkable grain growth in comparison with the SZ and the TMAZ. The grain growth recorded in this zone (for configuration 2) was attributed, on the one hand, to the direct contact between the Cu sheet and the tool shoulder and, on the other hand, to the excellent thermal conductivity of Cu. Few annealing twins are also observed in this region.

The different welding regions described before could not be distinguished in the Al sheet for this configuration due to the non-occurrence of the stirring. This was attributed to the thermomechanical induced softening of the Al material and stretching deformation of the interface under the high pressure of the pin. For this configuration, only the TMAZ and the HAZ were observed. Their microstructures were similar to those presented in Fig. 10c and e and are not given here for reasons of conciseness. The microstructural characteristics and material flow, observed in this study, are in good agreement with those published in other research works [48–52].

Fig. 10 Optical micrographs (for configuration #1), respectively: **a** SZ, **c** TMAZ, and **e** HAZ for Al material and **b** SZ, **d** TMAZ, and **f** HAZ for Cu material



The X-ray diffractograms of the P6 sample (configuration #1) are given in Fig. 12a, b. In addition to the presence of Al and Cu peaks, both Al_4Cu_9 and Al_2Cu peaks were also observed at the weld interface of the FSSW joint conducted without Zn interlayer (Fig. 12a). The diffractograms of the FSSW joint containing Zn interlayer (Fig. 12b) show the presence of $Al_{4.2}Cu_{3.2}Zn_{0.7}$ ternary compound peaks. No Al_4Cu_9

peaks were detected in this case. Similar results were found in the diffractograms corresponding to configuration #2. The figures are not presented for reasons of conciseness.

Figure 13a–d shows SEM micrographs of the cross sections taken from Fig. 5a and b for configuration #1. Figure 13a illustrates the SEM image observed in region 1 of Fig. 5b. It shows the presence of large particle fragments

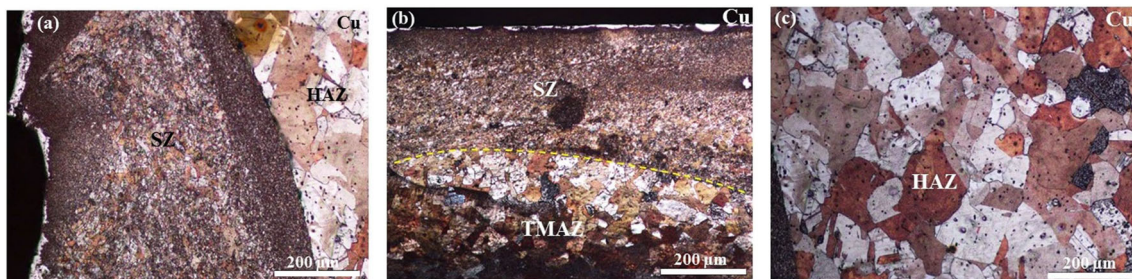


Fig. 11 Optical micrographs of the Cu material (configuration #2). **a** SZ, **b** TMAZ, and **c** HAZ

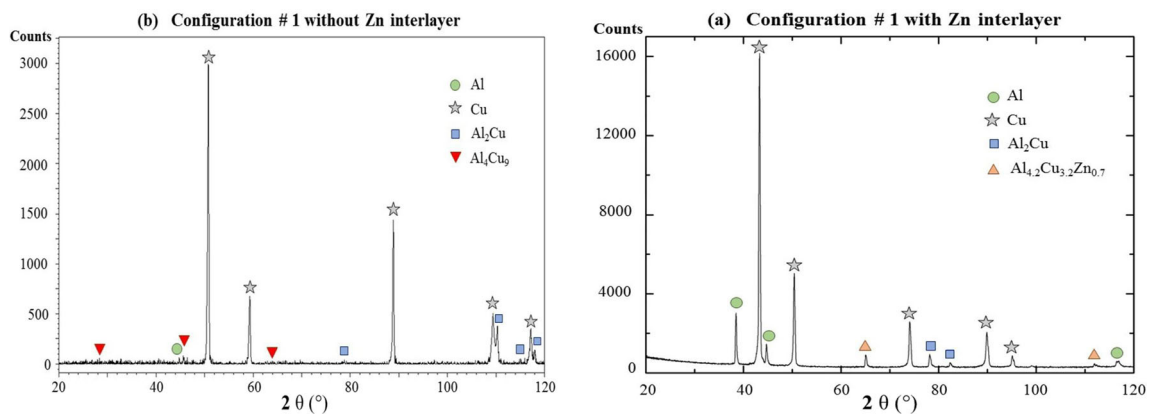
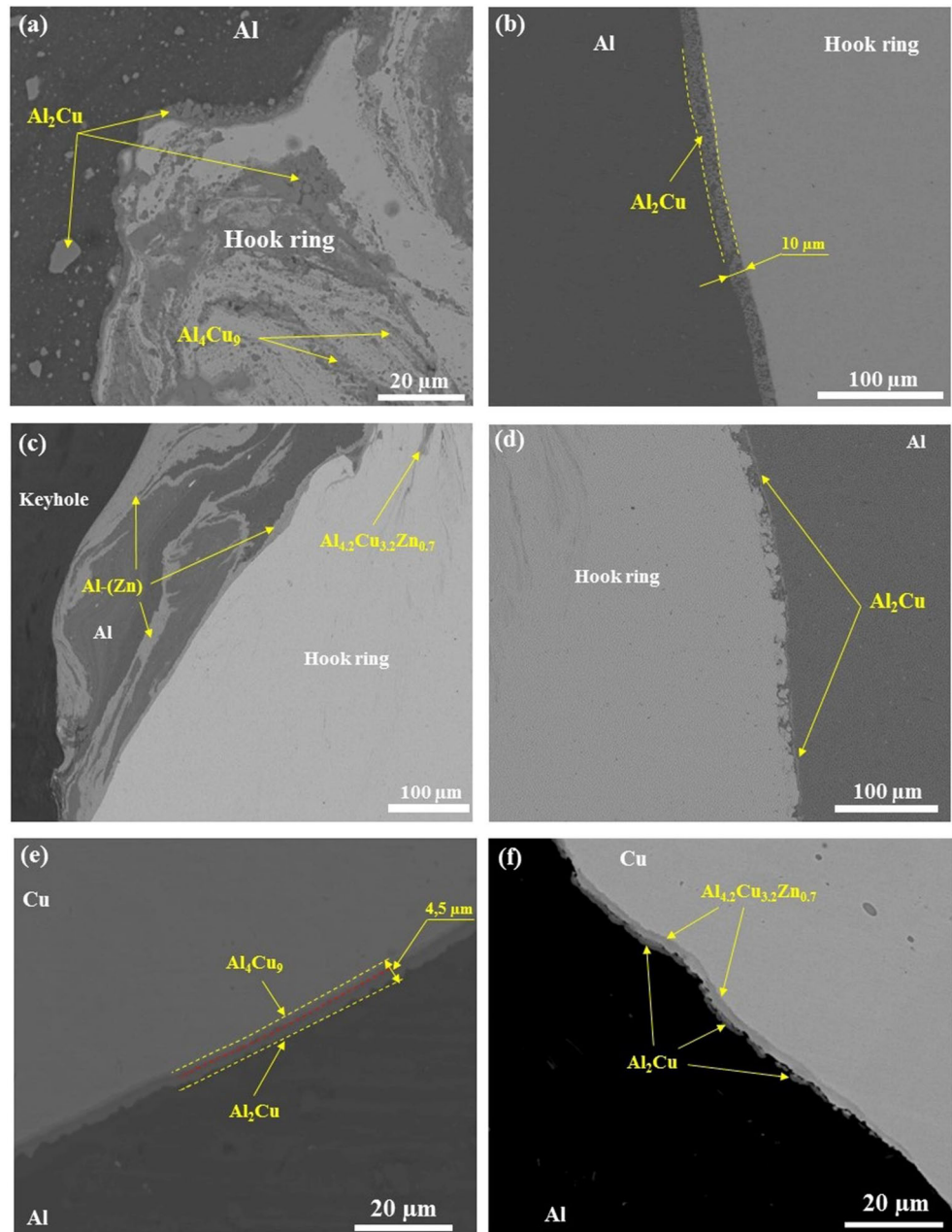


Fig. 12 X-ray diffractograms (for configuration #1) measured at the weld interface **a** with Zn interlayer and **b** without Zn interlayer

Fig. 13 BSE-SEM micrographs for different regions of Al/Cu interface. **a** and **b** Marked regions 1 and 2 on Fig. 5b, **c** and **d** marked regions 3 and 4 on Fig. 5a, **e** and **f** marked regions 5 and 6 on Fig. 5j and i respectively



of Cu with irregular sizes scattered and diffused in the Al matrix. These particles correspond to the IMCs created near the hook ring due to the increased mechanical stirring effect along the Al/Cu interface. Similar results were published by Heideman et al. [11] and Mubiayi et al. [12]. According to EDS analysis results, the precipitates observed in this figure correspond to Al_4Cu_9 and Al_2Cu (see Table 3 for the chemical compositions). Figure 13b shows an SEM image observed in region 2 of Fig. 5b. It shows the presence of continuous layer (of about 10 μm thickness) formed along the Al/Cu interface. EDS analysis confirmed that this layer corresponds to Al_2Cu IMC. Figure 13c and d show SEM images observed respectively in regions 3 and 4 of Fig. 5a for configuration #1. The thermomechanical effect of the FSSW process caused the melting of the introduced Zn interlayer and the dispersion of its particles throughout Al and Cu sheets. EDS analysis revealed the presence of an interdiffusion region that was composed of Al-(Zn) solid solution as shown in Fig. 13c. These results are supported by those published by Mokabberi et al. [53]. In the swirl flow (top of the hook), EDS analysis indicated the presence of $\text{Al}_{4.2}\text{Cu}_{3.2}\text{Zn}_{0.7}$ IMC (see Table 3 for its chemical composition).

As shown in Fig. 13d, the layer located near the Al sheet corresponds to thin Al_2Cu precipitates of about 2.07 μm thick. Gaohui et al. [9] attributed the formation of these precipitates in FSSW joints to the dwell time effect. It should be noted that the introduction of the Zn foil at the Al/Cu interface reduced remarkably the thickness of the continuous IMC layer, from 10 to 2 μm (Fig. 13b and d). It also reduced the width of the hook ring, known to favor the crack propagation, as described before in Fig. 5 (a–d). These results are well supported by the work published by Elrefaey et al. [29] who noticed that the Zn introduction in Al/Cu FSW lap joints suppressed the formation of the Cu fragments. Figure 13e shows the SEM image observed in region 5 of Fig. 5j (configuration #2 without Zn). It indicates the presence of thick intermetallic layer along the Cu/Al interface. EDS analysis confirmed that this layer was mainly composed of both Al_2Cu and Al_4Cu_9 precipitates. A previous study [15] showed that, during dissimilar FSSW of Cu and Al, the Al_2Cu and Al_4Cu_9 layers dominated the microstructures of Al and Cu respectively. Abbasi et al. [7]

noticed that Al_2Cu had higher size than Al_4Cu_9 due to the higher activation diffusion energy of Cu in Al. Figure 13f shows the SEM image taken in region 6 of Fig. 5i (configuration #2 with Zn) highlights the presence of discontinuous Al_2Cu (for the Al sheet) and $\text{Al}_{4.2}\text{Cu}_{3.2}\text{Zn}_{0.7}$ (for Cu sheet). The introduction of Zn interlayer suppressed the formation of brittle Al_4Cu_9 IMC at the Cu/Al interface and favored the formation of the ternary $\text{Al}_{4.2}\text{Cu}_{3.2}\text{Zn}_{0.7}$ (τ') phase. This is due to the chemical affinity between Cu and Zn. Indeed, during the FSSW process, the Al-Zn-Cu reaction could occur through two ways: Firstly, when the Zn foil is melted due to its low fusion point, it reacts with Cu. Simultaneously, the Al react with Cu due to their relatively high electronegativity. This favors the formation of $\text{Al}_{4.2}\text{Cu}_{3.2}\text{Zn}_{0.7}$ ternary compound. Secondly, owing to the consumption of Zn atoms during the reaction with Cu at the interface, Cu and Al react to form Al_2Cu layer at the Al/Cu interface. Several studies [20, 54] explained that the $\text{Al}_{4.2}\text{Cu}_{3.2}\text{Zn}_{0.7}$ ternary compound serves as a good diffusion barrier against the formation of harmful Al_4Cu_9 IMC. In addition, the AlCu , Al_4Cu_3 , Al_2Cu_3 , and AlCu_3 brittle IMCs, which were often found in other research works [7, 10, 16, 19], were not observed in the present study for both configurations #1 and #2 with Zn interlayer. These results are well supported by the works of Balasundaram et al. [27] and Boucherit et al. [54] who noticed the absence of Al_4Cu_9 in Al/Cu weld joints containing Zn interlayer. It should be noticed that, for both configurations #1 and #2, the introduction of Zn interlayer reduced sensibly the thickness of the intermetallic layer. In addition, the presence of thin continuous intermetallic layer at the spot weld interface improves their tensile strength as reported previously [9, 55]. However, thick continuous IMCs whose thickness exceed 3 μm had a harmful effect on the weld joint quality as reported by Lee et al. [18], Zhou et al. [56], and Solchenbach et al. [57].

3.3 Microhardness evolution around the keyhole

The Vickers microhardness maps in the transverse sections of the P6-Zn #1 and P6-Zn #2 joints are depicted in Fig. 14a, b. It can be easily noticed that the different regions the weld joint

Table 3 EDS analyses results of the different precipitates at the spot weld interface according to Fig. 13

| Phases | Element content (at.%) | | | Configuration | Corresponding figures |
|---|------------------------|-------|-------|---------------|-----------------------|
| | Al | Cu | Zn | | |
| Al_2Cu | 68.25 | 31.75 | - | #1 and #2 | Figure 13a, b, and e |
| | 66.90 | 30.88 | 2.22 | #1 and #2 | Figure 13d and f |
| Al_4Cu_9 | 28.85 | 71.15 | - | #1 and #2 | Figure 13a and e |
| Al-(Zn) solid solution | 73.71 | 3.61 | 22.68 | #1 | Figure 13c |
| $\text{Al}_{4.2}\text{Cu}_{3.2}\text{Zn}_{0.7}$ | 52.05 | 34.16 | 13.79 | #1 and #2 | Figure 13c and f |

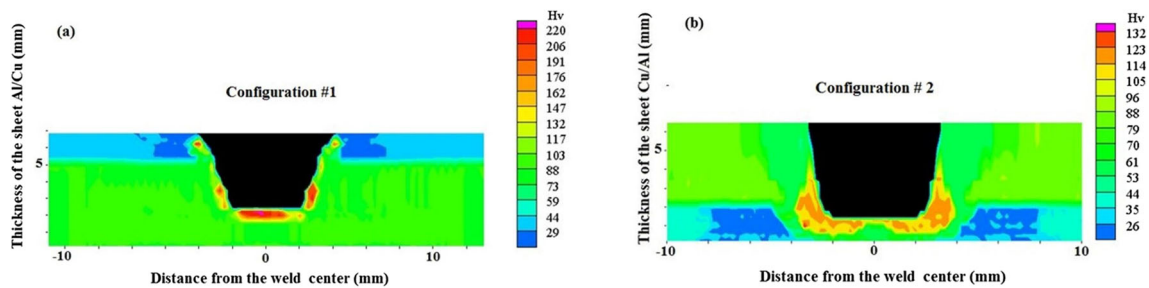


Fig. 14 Microhardness mapping across the FSSW joint made using 6 mm pin length and Zn interlayer. **a** Configuration #1. **b** Configuration #2

issued from configuration 1 (Fig. 14a) exhibit high microhardness level in comparison with configuration 2 (Fig. 14b).

In addition, the SZ exhibited the highest microhardness values (228 HV). This was attributed to its fine grain microstructure according to the Hall-Petch relationship [56, 58]. In addition, the high hardness level of the SZ can be related to the presence of the different types of IMCs described above in Fig. 13. Similar statements were reported by several authors [18, 56]. Besides, the increase of the microhardness around the keyhole may be explained by the presence of an interdiffusion band as reported by Kuang et al. [59]. According to Gaohui et al. [9], the high microhardness level around the keyhole was attributed to the dispersion of hard IMC particles. These authors explained that the presence of uniform IMC layer, at the weld interface with an optimized thickness, improved its mechanical properties. It should be noted that the lowest microhardness values were recorded in the HAZ due, on the one hand, to the grain growth that occurred in this region and, on the other hand, to the material softening induced by the weld thermal cycles. The difference in the maximum hardness level between configurations 1 and 2 can be attributed, on the one hand, to the Zn melting and precipitated IMCs and, on the other hand, to the lack of materials' stirring in the case of configuration 2 as described above in Fig. 5i–j. In fact, because of the Cu sheet thickness (5 mm), the Zn foil was squeezed out of the sheet interface as described earlier in Fig. 5j and the Al sheet was stamped without intermingling with Cu in the SZ. This resulted in the low hardness level recorded in the SZ of the configuration 2 despite its fine grain microstructure. According to the map given in Fig. 14b, the microhardness values varied between 19 and 140 $HV_{0.05}$. The SZ was characterized by high microhardness level as indicated previously. The HAZ microhardness ranged between 50 and 65 $HV_{0.05}$ for Cu and between 19 and 26 HV for Al. These results are in good agreement with those reported in other research works [13, 56].

3.4 Residual stress analysis

Figure 15a–d illustrates the longitudinal and transversal RS distributions for the investigated configurations conducted with and without Zn interlayer. For both configurations, the

RSs were reinforced at the HAZ/SZ interface because of the intense thermal gradient, the significant deformation, and the phase transformations between the Al and Cu materials. The obtained RSs were of compressive type in the SZ and of tensile type in the HAZ. In the transverse direction, weak tensile stresses were created in comparison with the longitudinal direction.

The highest values of the longitudinal RS (Fig. 15a, c) were recorded around the spot weld center (at a distance comprised between 5 and 7 mm from the weld center), whereas the transversal RS (Fig. 15b, d) exhibited low values and were generally of compressive type. Besides, the Zn addition decreased the RS distribution across the spot weld joint. For configuration #1, the longitudinal RS profile decreased close to the spot weld center (Fig. 15a, b). As described above, the Zn introduction improved the ductility of the spot weld joint and favored the good bonding of the materials at the weld interface. This was also enhanced by the formation of thin continuous intermetallic layer. The longitudinal RSs distribution were quasi-symmetric in configuration #1 with Zn interlayer (Fig. 15a) and a weak tensile RS value of +20 MPa was recorded in the HAZ. Weak compressive longitudinal stresses were also recorded in this case. The spot welds realized without Zn interlayer exhibited higher RSs in the HAZ with an average value of 35 MPa. Figure 15b indicates the presence of low compressive transversal RSs with amplitude between –10 and –30 MPa. The presence of this type of RS may be explained by the nature of the FSSW process that had no strong effect on the welded sheets in the transversal direction. For configuration #2 (Fig. 15c), the maximum RS value (close to +60 MPa) was recorded in the HAZ of the spot weld realized without Zn interlayer. This confirms the effect of Zn interlayer addition on the mechanical properties evolution described above. In fact, the Zn addition contributed to the change of the longitudinal RS state across the FSSW joint from tensile to compressive type with a maximal value of –60 MPa in the HAZ. Figure 15d shows the distribution of the transversal RS across the spot welds issued from configuration #2. For the spot welds conducted without Zn addition, compressive RSs of –10 MPa and –50 MPa were recorded in the SZ and the HAZ respectively. However, the FSSW joints containing Zn interlayer exhibited tensile RSs of +5 MPa

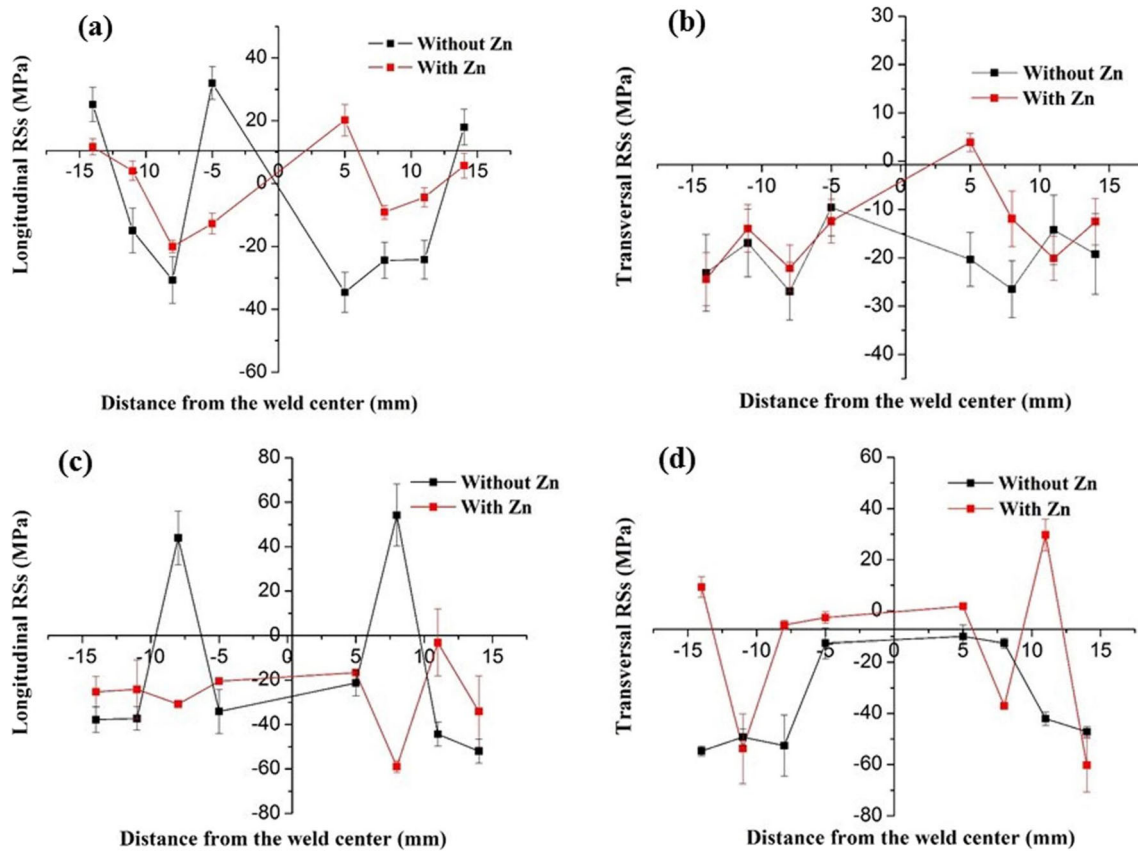


Fig. 15 Residual stresses distribution across the FSSW joint. **a** Longitudinal RSs and **b** transversal RSs for configuration #1. **c** Longitudinal RSs and **d** transversal RSs for configuration #2

and +30 MPa in the SZ and the HAZ respectively. The high longitudinal RS value recorded in the case of configuration #2 can be explained by the discontinuous character and the size of the intermetallic compounds described above. In addition, the grain size values recorded in the HAZ for this configuration that are higher than those obtained in the case of configuration #1 contributed to the RS increase in this region. This result can be attributed to the decrease of the grain interface density which could enhance the recorded decrease in microhardness values. The RSs' decrease in the SZ can be attributed to its improved microhardness resulting from the fine grain microstructure according to the Hall-Petch mechanism [58, 60]. It is known that the yield stress increase leads to RSs' decrease [34], since microhardness is directly related to the yield stress [61, 62], thus, the RSs evolution obtained in this work can be attributed to the microhardness evolution across the FSSW joints. It should be noted that the important hook ring size obtained in configuration #1 contributed significantly to the improvement of the mechanical properties (paragraph 3.1) through the decrease of the RS amplitude. It is clear that the use of Zn interlayer (Fig. 15a–d) weakened the compressive RS. This result could be explained by the formation of intermetallic phases at the spot weld interfaces during processing as mentioned above.

4 Conclusions

The dissimilar friction stir spot welding of Al and Cu was conducted through two different configurations using Zn interlayer. The main conclusions of this research are summarized as follows:

- The spot weld interface was strongly dependent on the configuration type. In configuration #1, the location of Al sheet in the upper position of the lap joint favored the Cu extrusion upwards into the Al sheet and enhanced a good intermixing at the weld interface. This promoted the creation of a conical hook ring around the keyhole that had a beneficial effect on the weld joint quality. Conversely, in configuration #2, despite the sufficient pin length, the good stirring at the weld interface could not be achieved because of the malleability of Al sheet. A stamped morphology, resulting from both the strong plastic deformation and the excessive heat input, was obtained in this case.
- For both configurations, the spot weld joint quality was sensibly influenced by the pin length and the Zn addition. The best tensile properties (tensile shear strength and elongation) corresponded to the longest used pin (6 mm). The introduction of Zn interlayer increased the tensile shear

strength of about 118% and 53% for configurations #1 and #2 respectively.

- Complex precipitation phenomena were recorded around the keyhole for the weld joints realized without Zn interlayer. The introduction of this element at the weld interface reduced sensibly the width of Al₂Cu layer and favored the precipitation of the Al_{4.2}Cu_{3.2}Zn_{0.7} IMC. This later prevented the formation of the detrimental Al₄Cu₉ layers.
- The presence of an intermixing zone with fine grain microstructure containing thin continuous intermetallic layer and Zn fragments around the hook ring (configuration #1) resulted in a high hardness level at the Al/Cu interface. Conversely, in configuration #2, the Zn foil was squeezed out of the sheet interface resulting in the absence of material intermixing and low microhardness level. The lowest microhardness values were obtained in the HAZ due to the grain growth phenomenon.
- Both configuration type and Zn addition affected the RSs distribution across the spot weld joint. Configuration #1 produced quasi-symmetric distribution of weak compressive and tensile RSs. Besides, the use of Zn interlayer in this configuration reduced the RS state across the FSSW joint. This promoted its good mechanical properties in comparison with the FSSW joints obtained from configuration #2.
- The experimental investigations conducted in this work recommend the use of Zn interlayer and the location of the aluminum in the upper position of the FSSW lap joint and the copper in the lower one for joining these materials.

Funding This study was financially supported by the Research Center in Industrial Technologies (CRTI).

Data availability The raw/processed data required to reproduce these findings cannot be shared at this time as they will be used in an ongoing study.

References

1. de la Parte MP et al (2020) A new way to predict the mechanical properties of friction stir spot welding for Al-Cu joints by energy analysis of the vibration signals. *Int J Adv Manuf Technol* 105: 1823–1834. <https://doi.org/10.1007/s00170-019-04396-5>
2. Sarvghad-moghaddam M, Parvizi R, Davoodi A, Haddad-sabzevar M, Imani A (2014) Establishing a correlation between interfacial microstructures and corrosion initiation sites in Al/Cu joints by SEM-EDS and AFM-SKPFM. *Corros Sci* 79:148–158. <https://doi.org/10.1016/j.corsci.2013.10.039>
3. Garg A, Bhattacharya A (2020) Friction stir spot welding of AA6061-T6 and Cu with preheating: strength and failure behavior at different test temperatures. *Int J Adv Manuf Technol* 108:1613–1629. <https://doi.org/10.1007/s00170-020-05498-1>
4. Li X, Zhang D, Qiu C, Zhang W (2012) Microstructure and mechanical properties of dissimilar pure copper/1350 aluminum alloy butt joints by friction stir welding. *Trans Nonferrous Metals Soc China* 22:1298–1306. [https://doi.org/10.1016/S1003-6326\(11\)61318-6](https://doi.org/10.1016/S1003-6326(11)61318-6)
5. Liu P, Shi Q, Wang W, Wang X, Zhang Z (2008) Microstructure and XRD analysis of FSW joints for copper T2/aluminium 5A06 dissimilar materials. *Mater Lett* 62:4106–4108. <https://doi.org/10.1016/j.matlet.2008.06.004>
6. Ni ZL, Ye FX (2016) Weldability and mechanical properties of ultrasonic joining of aluminum to copper alloy with an interlayer. *Mater Lett* 182:19–22. <https://doi.org/10.1016/j.matlet.2016.06.071>
7. Abbasi M, Karimi Taheri A, Salehi MT (2001) Growth rate of intermetallic compounds in Al/Cu bimetal produced by cold roll welding process. *J Alloys Compd* 319:233–241. [https://doi.org/10.1016/S0925-8388\(01\)00872-6](https://doi.org/10.1016/S0925-8388(01)00872-6)
8. Pandey AK, Chatterjee S, Mahapatra SS (2019) Analysis and characterization of weld quality during butt welding through friction stir welding. *Indian J Eng Mater Sci* 26:298–310 <http://nopn.niscair.res.in/handle/123456789/53512>
9. Li G, Zhou L, Zhou W, Song X, Huang Y (2019) Influence of dwell time on microstructure evolution and mechanical properties of dissimilar friction stir spot welded aluminum-copper metals. *J Mater Res Technol* 8(3):2613–2624. <https://doi.org/10.1016/j.jmrt.2019.02.015>
10. Shiraly M, Shamanian M, Toroghinejad MR, Ahmadi Jazani M (2014) Effect of tool rotation rate on microstructure and mechanical behavior of friction stir spot-welded Al/Cu composite. *J Mater Eng Perform* 23:413–420. <https://doi.org/10.1007/s11665-013-0768-8>
11. Heideman R, Johnson C, Kou S (2010) Metallurgical analysis of Al/Cu friction stir spot welding. *Sci Technol Weld Join* 15:597–605. <https://doi.org/10.1179/136217110X12785889549985>
12. Mubiayi MP, Akinlabi ET (2016) Evolving properties of friction stir spot welds between AA1060 and commercially pure copper C11000. *Trans Nonferrous Metals Soc China* 26:1852–1862. [https://doi.org/10.1016/S1003-6326\(16\)64296-6](https://doi.org/10.1016/S1003-6326(16)64296-6)
13. Galvão I, Oliveira JC, Loureiro A, Rodrigues DM (2012) Formation and distribution of brittle structures in friction stir welding of aluminium and copper: influence of shoulder geometry. *Intermetallics* 22:122–128. <https://doi.org/10.1016/j.intermet.2011.10.014>
14. Akinlabi ET, Andrews A, Akinlabi SA (2014) Effects of processing parameters on corrosion properties of dissimilar friction stir welds of aluminium and copper. *Trans Nonferrous Metals Soc China* 24: 1323–1330. [https://doi.org/10.1016/S1003-6326\(14\)63195-2](https://doi.org/10.1016/S1003-6326(14)63195-2)
15. Xue P, Xiao BL, Ni DR, Ma ZY (2010) Enhanced mechanical properties of friction stir welded dissimilar Al-Cu joint by intermetallic compounds. *Mater Sci Eng A* 527:5723–5727. <https://doi.org/10.1016/j.msea.2010.05.061>
16. Abdollah-Zadeh A, Saeid T, Sazgari B (2008) Microstructural and mechanical properties of friction stir welded aluminum/copper lap joints. *J Alloys Compd* 460:535–538. <https://doi.org/10.1016/j.jallcom.2007.06.009>
17. Xu WF, Liu JH, Chen DL (2011) Material flow and core/multi-shell structures in a friction stir welded aluminum alloy with embedded copper markers. *J Alloys Compd* 509:8449–8454. <https://doi.org/10.1016/j.jallcom.2011.05.118>
18. Lee W, Bang K, Jung S (2005) Effects of intermetallic compound on the electrical and mechanical properties of friction welded Cu/Al bimetallic joints during annealing. *J Alloys Compd* 390:212–219. <https://doi.org/10.1016/j.jallcom.2004.07.057>
19. Tan CW, Jiang ZG, Li LQ, Chen YB, Chen XY (2013) Microstructural evolution and mechanical properties of dissimilar Al-Cu joints produced by friction stir welding. *Mater Des* 51:466–473. <https://doi.org/10.1016/j.matdes.2013.04.056>
20. Zhang J, Shen Y, Yao X, Xu H, Li B (2014) Investigation on dissimilar underwater friction stir lap welding of 6061-T6

- aluminum alloy to pure copper. *Mater Des* 64:74–80. <https://doi.org/10.1016/j.matdes.2014.07.036>
21. Xue P, Ni DR, Wang D, Xiao BL, Ma ZY (2011) Effect of friction stir welding parameters on the microstructure and mechanical properties of the dissimilar Al–Cu joints. *Mater Sci Eng A* 528:4683–4689. <https://doi.org/10.1016/j.msea.2011.02.067>
 22. Xiao Y, Ji H, Li M, Kim J (2013) Ultrasound-assisted brazing of Cu/Al dissimilar metals using a Zn–3Al filler metal. *Mater Des* 52:740–747. <https://doi.org/10.1016/j.matdes.2013.06.016>
 23. Saeid T, Abdollah-zadeh A, Sazgari B (2010) Weldability and mechanical properties of dissimilar aluminum–copper lap joints made by friction stir welding. *J Alloys Compd* 490:652–655. <https://doi.org/10.1016/j.jallcom.2009.10.127>
 24. Dai W, Xue SB, Lou JY, Lou YB, Wang SQ (2012) Torch brazing 3003 aluminum alloy with Zn–Al filler metal. *Trans Nonferrous Metals Soc China* 22:30–35. [https://doi.org/10.1016/S1003-6326\(11\)61135-7](https://doi.org/10.1016/S1003-6326(11)61135-7)
 25. Andrade-gamboa A, Gennari FC, Larochette PA, Neyertz C, Ahlers M, Pelegrina JL (2007) Stability of Cu–Zn phases under low energy ball milling. *Mater Sci Eng A* 447:324–331. <https://doi.org/10.1016/j.msea.2006.10.134>
 26. Feng J, Songbai X (2013) Growth behaviors of intermetallic compound layers in Cu/Al joints brazed with Zn–22Al and Zn–22Al–0.05Ce filler metals. *Mater Des* 51:907–915. <https://doi.org/10.1016/j.matdes.2013.04.069>
 27. Balasundaram R, Patel VK, Bhole SD, Chen DL (2014) Effect of zinc interlayer on ultrasonic spot welded aluminum-to-copper joints. *Mater Sci Eng A* 607:277–286. <https://doi.org/10.1016/j.msea.2014.03.135>
 28. Feng JI, Song-bai XUE, Ji-yuan LOU, Yin-bin LOU, Shui-qing W (2012) Microstructure and properties of Cu/Al joints brazed with Zn–Al filler metals. *Trans Nonferrous Metals Soc China* 22:281–287. [https://doi.org/10.1016/S1003-6326\(11\)61172-2](https://doi.org/10.1016/S1003-6326(11)61172-2)
 29. Elrefaey A, Takahashi M, Ikeuchi K (2005) Preliminary investigation of friction stir welding aluminium/copper lap joints. *Weld World* 49:93–101. <https://doi.org/10.1007/BF03266481>
 30. Chang WS, Rajesh SR, Chun CK, Kim H-J (2011) Microstructure and mechanical properties of hybrid laser–friction stir welding between AA6061–T6 Al alloy and AZ31 Mg alloy. *J Mater Sci Technol* 27:199–204. [https://doi.org/10.1016/S1005-0302\(11\)60049-2](https://doi.org/10.1016/S1005-0302(11)60049-2)
 31. Chatterjee S, Pandey AK, Mahapatra SS, Arora KS, Behera A (2020) Microstructural variation at interface during fiber laser joining of NiTi/Ti6Al4V and effect of mechanical strength. *J Mater Process Technol* 282:116661. <https://doi.org/10.1016/j.jmatprotec.2020.116661>
 32. Chatterjee S, Mahapatra SS, Arora KS, Behera A (2020) Physical and mechanical characterization of dissimilar laser welded joints of AISI 316/Cu/SMA using fiber laser technology. *J Laser Appl* 32:p032018. <https://doi.org/10.2351/7.0000003>
 33. Aissani M, Gachi S, Bounider F, Benkedda Y (2010) Design and optimization of friction stir welding tool. *Mater Manuf Process* 11:1199–1205. <https://doi.org/10.1080/10426910903536733>
 34. Mehdi B, Badji R, Ji V, Allili B, Bradai D, Deschaux-beaume F, Soulié F (2016) Microstructure and residual stresses in Ti–6Al–4V alloy pulsed and unpulsed TIG welds. *J Mater Process Technol* 231:441–448. <https://doi.org/10.1016/j.jmatprotec.2016.01.018>
 35. Lebrun M. Norme Européenne NF EN 15305. 2009. www.afnor.org
 36. Tran V, Pan J, Pan T (2008) Fatigue behavior of aluminum 5754-O and 6111-T4 spot friction welds in lap-shear specimens. *Int J Fatigue* 30:2175–2190. <https://doi.org/10.1016/j.ijfatigue.2008.05.025>
 37. Shen Z, Yang X, Zhang Z, Cui L, Yin Y (2013) Mechanical properties and failure mechanisms of friction stir spot welds of AA 6061-T4 sheets. *Mater Des* 49:181–191. <https://doi.org/10.1016/j.matdes.2013.01.066>
 38. Zhang Z, Yang X, Zhang J, Zhou G, Xu X, Zou B (2011) Effect of welding parameters on microstructure and mechanical properties of friction stir spot welded 5052 aluminum alloy. *Mater Des* 32:4461–4470. <https://doi.org/10.1016/j.matdes.2011.03.058>
 39. Rao HM, Jordon JB, Barkey ME, Guo YB, Su X, Badarinarayan H (2013) Influence of structural integrity on fatigue behavior of friction stir spot welded AZ31 Mg alloy. *Mater Sci Eng A* 564:369–380. <https://doi.org/10.1016/j.msea.2012.11.076>
 40. Sun YF, Shen JM, Morisada Y, Fujii H (2014) Spot friction stir welding of low carbon steel plates preheated by high frequency induction. *Mater Des* 54:450–457. <https://doi.org/10.1016/j.matdes.2013.08.071>
 41. Zhao YY, Li D, Zhang YS (2013) Effect of welding energy on interface zone of Al–Cu ultrasonic welded joint. *Sci Technol Weld Join* 18:354–360. <https://doi.org/10.1179/1362171813Y.0000000114>
 42. Han B, Huang Y, Lv S, Wan L, Feng J, Fu G (2013) AA7075 bit for repairing AA2219 keyhole by filling friction stir welding. *Mater Des* 51:25–33. <https://doi.org/10.1016/j.matdes.2013.03.089>
 43. Mimouni O, Badji R, Kouadri-David A, Gassaa R, Chekroun N, Hadji M (2019) Microstructure and mechanical behavior of friction-stir-welded 2017A–T451 aluminum alloy. *Trans Indian Inst Metals* 72:1853–1868. <https://doi.org/10.1007/s12666-019-01663-7>
 44. Huang K, Logé RE (2016) A review of dynamic recrystallization phenomena in metallic materials. *Mater Des* 111:548–574. <https://doi.org/10.1016/j.matdes.2016.09.012>
 45. Sato YS, Park SHC, Kokawa H (2001) Microstructural factors governing hardness in friction-stir welds of solid-solution-hardened Al alloys. *Metall Mater Trans A* 32:3033–3042. <https://doi.org/10.1007/s11661-001-0178-7>
 46. Su JQ, Nelson TW, Mishra R, Mahoney M (2003) Microstructural investigation of friction stir welded 7050–T651 aluminium. *Acta Mater* 51:713–729. [https://doi.org/10.1016/S1359-6454\(02\)00449-4](https://doi.org/10.1016/S1359-6454(02)00449-4)
 47. Mroczka K, Dutkiewicz J, Pietras A (2010) Microstructure of friction stir welded joints of 2017A aluminium alloy sheets. *J Microsc* 237:521–525. <https://doi.org/10.1111/j.1365-2818.2009.03319.x>
 48. Yang Q, Mironov S, Sato YS, Okamoto K (2010) Material flow during friction stir spot welding. *Mater Sci Eng A* 527:4389–4398. <https://doi.org/10.1016/j.msea.2010.03.082>
 49. Su P, Gerlich A, Yamamoto M, North TH (2007) Formation and retention of local melted films in AZ91 friction stir spot welds. *J Mater Sci* 42:9954–9965. <https://doi.org/10.1007/s10853-007-2061-4>
 50. Lin Y, Liu J, Chen J (2013) Material flow tracking for various tool geometries during the friction stir spot welding process. *J Mater Eng Perform* 22:3674–3683. <https://doi.org/10.1007/s11665-013-0680-2>
 51. Badarinarayan H, Shi Y, Li X, Okamoto K (2009) Effect of tool geometry on hook formation and static strength of friction stir spot welded aluminum 5754-O sheets. *Int J Mach Tools Manuf* 49:814–823. <https://doi.org/10.1016/j.ijmactools.2009.06.001>
 52. Jeon C, Hong S, Kwon Y, Cho H, Han HN (2012) Material properties of friction stir spot welded joints of dissimilar aluminum alloys. *Trans Nonferrous Metals Soc China* 22:605–613. [https://doi.org/10.1016/S1003-6326\(12\)61772-5](https://doi.org/10.1016/S1003-6326(12)61772-5)
 53. Mokabberi SR, Movahedi M, Kokabi AH (2018) Effect of interlayers on softening of aluminum friction stir welds. *Mater Sci Eng A* 727:1–10. <https://doi.org/10.1016/j.msea.2018.04.093>
 54. Boucherit A, Avettand-fénoël MN, Taillard R (2017) Effect of a Zn interlayer on dissimilar FSSW of Al and Cu. *Mater Des* 124:87–99. <https://doi.org/10.1016/j.matdes.2017.03.063>

55. Yang JW, Cao B, He XC, Luo HS (2014) Microstructure evolution and mechanical properties of Cu–Al joints by ultrasonic welding. *Sci Technol Weld Join* 19:500–504. <https://doi.org/10.1179/1362171814Y.0000000218>
56. Zhou L, Zhang RX, Li GH, Zhou WL, Huang YX, Song XG (2018) Effect of pin profile on microstructure and mechanical properties of friction stir spot welded Al–Cu dissimilar metals. *J Manuf Process* 36:1–9. <https://doi.org/10.1016/j.jmapro.2018.09.017>
57. Solchenbach T, Plapper P (2013) Mechanical characteristics of laser braze-welded aluminium–copper connections. *Opt Laser Technol* 54:249–256. <https://doi.org/10.1016/j.optlastec.2013.06.003>
58. Lin Y, Liu J, Lin B, Lin C, Tsai H (2012) Effects of process parameters on strength of Mg alloy AZ61 friction stir spot welds. *Mater Des* 35:350–357. <https://doi.org/10.1016/j.matdes.2011.08.050>
59. Kuang B, Shen Y, Chen W, Yao X, Xu H, Gao J, Zhang J (2015) The dissimilar friction stir lap welding of 1A99 Al to pure Cu using Zn as filler metal with “pinless” tool configuration. *Mater Des* 68: 54–62. <https://doi.org/10.1016/j.matdes.2014.12.008>
60. Kherrouba N, Carron D, Bouabdallah M, Badji R (2019) Effect of solution treatment on the microstructure, micromechanical properties, and kinetic parameters of the $\beta \rightarrow \alpha$ phase transformation during continuous cooling of Ti–6Al–4V titanium alloy. *J Mater Eng Perform* 28:6921–6930. <https://doi.org/10.1007/s11665-019-04404-5>
61. Cahoon JR, Broughton WH, Kutzak AR (1971) The determination of yield strength from hardness measurements. *Metall Mater Trans B Process Metall Mater Process Sci* 2:1979–1983. <https://doi.org/10.1007/BF02913433>
62. Busby JT, Hash MC, Was GS (2005) The relationship between hardness and yield stress in irradiated austenitic and ferritic steels. *J Nucl Mater* 336:267–278. <https://doi.org/10.1016/j.jnucmat.2004.09.024>

Publisher's note Springer Nature remains neutral with regard to jurisdictional claims in published maps and institutional affiliations.